Observational evidence against mountain-wave generation of ice nuclei as a prerequisite for the formation of three solid nitric acid polar stratospheric clouds observed in the Arctic in early December 1999

Kathy L. Pagan,[1] Azadeh Tabazadeh,[2] Katja Drdla,[2] Mark E. Hervig,[3] Stephen D. Eckermann,[4] Edward V. Browell,[5] Marion J. Legg,[6] and Patricia G. Foschi[7]

Received 9 June 2003; revised 13 October 2003; accepted 16 December 2003; published 26 February 2004.

[1] A number of recently published papers suggest that mountain-wave activity in the stratosphere, producing ice particles when temperatures drop below the ice frost point, may be the primary source of large NAT particles. In this paper we use measurements from the Advanced Very High Resolution Radiometer (AVHRR) instruments on board the National Oceanic and Atmospheric Administration (NOAA) polar-orbiting satellites to map out regions of ice clouds produced by stratospheric mountain-wave activity inside the Arctic vortex. Lidar observations from three DC-8 flights in early December 1999 show the presence of solid nitric acid (Type Ia or NAT) polar stratospheric clouds (PSCs). By using back trajectories and superimposing the position maps on the AVHRR cloud imagery products, we show that these observed NAT clouds could not have originated at locations of high-amplitude mountain-wave activity. We also show that mountain-wave PSC climatology data and Mountain Wave Forecast Model 2.0 (MWFM-2) raw hemispheric ray and grid box averaged hemispheric wave temperature amplitude hindcast data from the same time period are in agreement with the AVHRR data. Our results show that ice cloud formation in mountain waves cannot explain how at least three large-scale NAT clouds were formed in the stratosphere in early December 1999. *INDEX TERMS:* 0320 Atmospheric Composition and Structure: Cloud physics and chemistry; 3334 Meteorology and Atmospheric Dynamics: Middle atmosphere dynamics (0341, 0342); 3360 Meteorology and Atmospheric Dynamics: Remote sensing; 3329 Meteorology and Atmospheric Dynamics: Mesoscale meteorology; 3349 Meteorology and Atmospheric Dynamics: Polar meteorology; *KEYWORDS:* AVHRR, NAT PSC formation mechanism, mountain wave cooling

Citation: Pagan, K. L., A. Tabazadeh, K. Drdla, M. E. Hervig, S. D. Eckermann, E. V. Browell, M. J. Legg, and P. G. Foschi (2004), Observational evidence against mountain-wave generation of ice nuclei as a prerequisite for the formation of three solid nitric acid polar stratospheric clouds observed in the Arctic in early December 1999, *J. Geophys. Res.*, *109*, D04312, doi:10.1029/2003JD003846.

1. Introduction

[2] Lidar observations show that both liquid (Type Ib) and solid (Type Ia) HNO_3-containing polar stratospheric cloud (PSC) particles are abundant in the winter polar stratosphere [*Browell et al.*, 1990; *Toon et al.*, 2000]. While the formation of liquid HNO_3-containing cloud particles in the stratosphere is now well understood, the nucleation mechanism for solid HNO_3 PSC formation still remains controversial [*World Meteorological Organization*, 2003]. Both homogeneous [*Salcedo et al.*, 2001; *Tabazadeh et al.*, 2001] and heterogeneous [*Tolbert and Toon*, 2001; *Drdla et al.*, 2003] freezing mechanisms have been suggested to account for the formation of solid nitric acid particles in the stratosphere. For standard homogenous and heterogeneous nucleation mechanisms to operate, the cooling caused by synoptic-scale uplift of air masses [*Teitelbaum et al.*, 2001; *Hitchman et al.*, 2003] can provide favorable conditions for solid nitric acid (NAT) clouds to form. In addition, *Carslaw et al.* [1998, 1999] have shown evidence for NAT cloud formation in air masses passing through regions of high-amplitude mountain-wave activity in the Arctic. NAT is assumed to nucleate heterogeneously on ice particles formed in mountain waves, leading to the release of small NAT particles when the ice evaporates in the warmer synoptic-scale temperatures downstream. If the synoptic-scale temperatures remain below the NAT threshold temperature, they can continue to take up HNO_3 and

[1]San Francisco State University, San Francisco, California, USA.
[2]NASA Ames Research Center, Moffett Field, California, USA.
[3]G & A Technical Software, Inc., Driggs, Idaho, USA.
[4]Naval Research Laboratory, Washington, DC, USA.
[5]NASA Langley Research Center, Hampton, Virginia, USA.
[6]Bay Area Environmental Research Institute, Sonoma, California, USA.
[7]Romberg Tiburon Center for Environmental Studies, San Francisco State University, Tiburon, California, USA.

Copyright 2004 by the American Geophysical Union.
0148-0227/04/2003JD003846$09.00

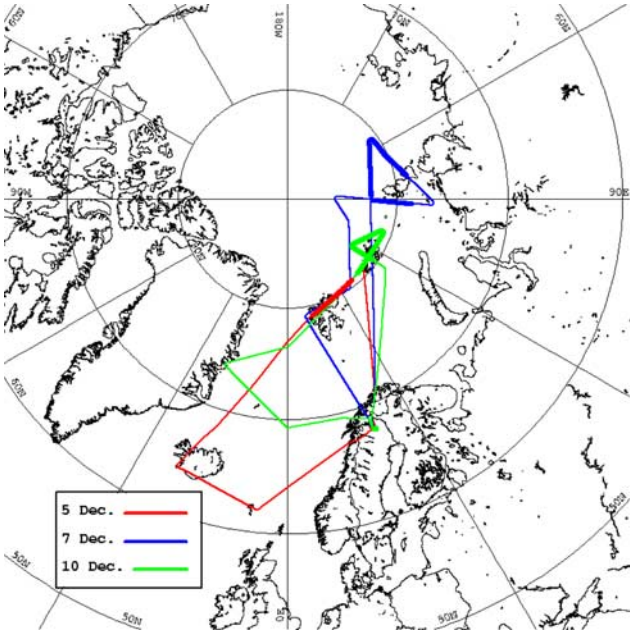

Figure 1. DC-8 flight paths for 5 December (red), 7 December (blue), and 10 December (green) 1999. The flight segments where the DC-8 DIAL lidar measured Type Ia PSCs are noted with a bold line.

H_2O and form NAT clouds. This process is described in detail by *Zondlo et al.* [2000]. A number of recent studies have provided additional support for the involvement of mountain-wave activity in the formation of NAT clouds in middle to late January 2000 within the Arctic vortex [*Fueglistaler et al.*, 2002a, 2002b; *Dhaniyala et al.*, 2002; *Luo et al.*, 2003; *Voight et al.*, 2003].

[3] Our approach in searching for the mechanism of NAT cloud formation described in this paper is novel. We use thermal infrared Advanced Very High Resolution Radiometer (AVHRR) data to map regions of ice PSCs formed by mountain-wave activity in the Arctic and then attempt to connect these regions (in time and space using trajectories) with regions where the DC-8 lidar observed NAT clouds. We also compare the AVHRR data with the location and timing of ice PSCs as predicted by the Mountain Wave Forecast Model Version 2 (MWFM-2). Our findings suggest that NAT clouds can indeed form in the stratosphere without ever passing through regions of mountain-wave activity. This is in agreement with an earlier analysis of Airborne Arctic Stratospheric Expedition (AASE) lidar observations of Type Ia PSCs by *Tabazadeh et al.* [1996]. However, our analysis cannot determine whether homogeneous nucleation or heterogeneous nucleation on particles other than ice was involved in causing the formation of these three NAT clouds in early December 1999 within the Arctic vortex.

[4] The article is organized as follows: In section 2, lidar data for the three NAT clouds observed on 5, 7, and 10 December 1999 are presented. In section 3, location and temperature histories of back trajectories calculated for each PSC event are shown. In section 4, the AVHRR ice PSC mapping algorithm is described and an ice PSC map is shown for the period 25 November to 10 December 1999. Back trajectory data are compared with the AVHRR ice PSC map to determine if the three NAT clouds were formed upstream in regions of mountain-wave activity with sufficient cooling to form ice PSCs. We also compare AVHRR ice PSC statistics for early December 1999 and January 2000 with mountain-wave ice PSC climatology statistics derived by *Dörnbrack and Leutbecher* [2001]. In section 5, we compare MWFM-2 hindcast data with the AVHRR ice PSC data and back trajectory data. Finally, in section 6, we present our conclusions and briefly discuss possible nucleation mechanisms that might account for the formation of the three NAT clouds observed in early December 1999.

2. DC-8 Lidar PSC Observations

[5] The NASA DC-8 made numerous flights in the Arctic region during the SAGE III Ozone Loss and Validation Experiment (SOLVE). The DC-8 Differential Absorption Lidar (DIAL) observed PSCs on 5, 7, and 10 December 1999, centered near 80°N and 24°E, 80°N and 105°E, and 81°N and 60°E, respectively. The DC-8 flight path and the PSC location for each of these three days are shown in Figure 1. These were large-scale PSCs, with areal extents, as measured along the DC-8 flight path, of approximately 500 km, 1405 km, and 992 km for 5, 7, and 10 December, respectively. All of these PSCs exhibited low scattering ratios and high depolarization ratios that are indicative of Type Ia (NAT) PSCs [*Browell et al.*, 1990]. Plots of the infrared depolarization ratios at 1064 nm in Figure 2 show the PSCs to be centered at ~20 to 22 km altitude with vertical extents of ~3 to 4 km.

[6] There were no DC-8 lidar measurements of ice PSCs in early December 1999. While the synoptic-scale temperatures were cold enough to sustain Type I PSCs, United Kingdom Meteorological Office (UKMO) analyses suggested that the synoptic conditions were too warm for ice PSC formation in early December 1999 [*Manney et al.*, 2003]. However, *Carslaw et al.* [1998, 1999], *Dörnbrack and Leutbecher* [2001], *Dörnbrack et al.* [2001] and others have shown that ice PSCs can form in the Arctic as a result of localized cooling associated with mesoscale mountain-wave activity. Therefore we used the locations of the DC-8 lidar Type Ia PSCs to initialize back trajectories for the three PSC events to determine whether the air parcels ever traveled through regions of mountain-wave activity prior to their detection.

3. Synoptic-Scale Back Trajectories

[7] We calculated 10-day back trajectories for the three NAT clouds observed in early December 1999 using the Goddard Space Flight Center (GSFC) isentropic trajectory model and 3.75° longitude × 2.50° latitude UKMO 1200 UTC temperature and wind data. We used the DC-8 lidar data to determine the starting points for the trajectories (15, 50, and 31 points for 5, 7, and 10 December, respectively) using a uniform grid (0.5 km vertical, 70 km horizontal) that covered the horizontal and vertical extent of each PSC. The synoptic-scale temperature history for each set of back trajectories is shown in Figure 3. The gray region in Figure 3 repre-

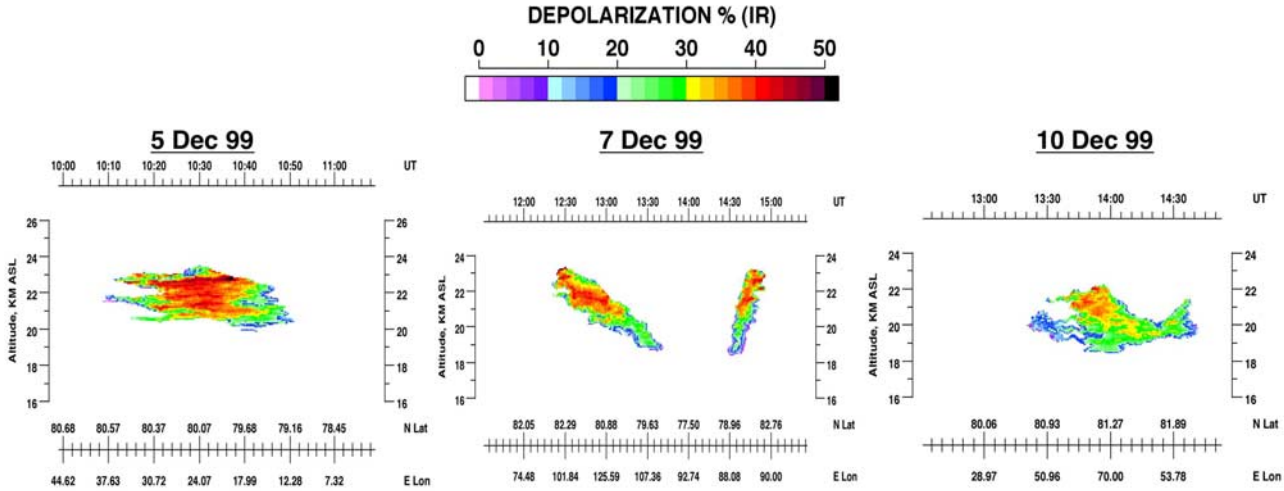

Figure 2. Infrared (1064 nm) DIAL lidar depolarization ratios for 5, 7, and 10 December 1999. High depolarization ratios and low scattering ratios (not shown) indicate these clouds were Type Ia (solid nitric acid) PSCs.

sents the range of synoptic-scale temperatures associated with all the trajectories, whereas the thick, colored line represents the mean synoptic-scale temperature history for each PSC event. The PSCs and the associated back trajectories were located in the region from ~30–50 hPa. The mean air parcel temperature for each PSC event cooled to below the NAT frost point (197.5 K at 50 hPa and 193.0 K at 30 hPa, assuming 10 ppbv HNO_3 and 5 ppmv H_2O) about 5 days prior to the lidar cloud measurements. At no time during the 10-day back trajectory period did the mean or minimum air parcel temperatures reach or drop below the ice frost point (188.4 K at 50 hPa and 185.5 K at 30 hPa, assuming 5 ppmv H_2O). Thus on the synoptic scale, there is no evidence that ice particles could have played a role in the formation of the Type Ia PSCs measured by the DC-8 lidar in early December 1999. This is in agreement with an analysis of synoptic-scale temperatures and PSC freezing processes by *Drdla et al.* [2003]. However, it is possible that cooling associated with mesoscale mountain-wave activity could lower the ambient air temperatures below the ice frost point. Therefore we compared the location of the back trajectories (Figure 5) with the AVHRR ice PSC map for the corresponding time period (Figure 4a) to determine if the air parcels traveled through regions of mountain-wave cloud activity at any time during the back trajectory period. The results of this comparison are discussed in the following section.

4. AVHRR Ice PSC Mapping

4.1. AVHRR Ice PSC Model

[8] The AVHRR instruments on board the National Oceanic and Atmospheric Administration (NOAA) polar-orbiting satellites have excellent spatial and temporal resolution at polar latitudes and have been collecting data continuously since 1979. The AVHRR is a five-channel, nadir-viewing, cross-track scanning radiometer with a horizontal resolution of 1.1 km at nadir [*Kidder and Vonder Haar*, 1995]. There are typically two AVHRR instruments in operation, and together they can collect upwards of eight passes per day for a given location at polar latitudes. The high spatial and temporal resolution of AVHRR data make them particularly useful for studying quickly evolving mesoscale wave-cloud events.

[9] *Pagan* [1996] and *Garcia et al.* [1995] determined that AVHRR channel 5 brightness temperatures (T_5) can be used to detect optically thick PSCs. *Foschi and Pagan* [2002] determined that the brightness temperature difference between AVHRR channels 4 and 5 (BTD) could be used to detect optically thin PSCs. Both of these studies concluded that the PSCs identified in AVHRR imagery were most likely composed of ice (Type II PSC). *Hervig et al.* [2001] developed a radiative transfer model that uses calibrated and georegistered AVHRR thermal infrared data (channel 4, 10.88 μm and channel 5, 11.94 μm) to identify PSCs. They simulated the AVHRR response to PSCs and concluded that Type I PSCs are invisible to AVHRR, whereas Type II (ice) PSCs are detectable for optical depths above ~0.05 to 0.10 for AVHRR thermal infrared wavelengths. They also determined that PSC and cirrus AVHRR signatures are similar, as they are both high, cold ice clouds. However, some differences between cirrus and PSCs exist; PSCs are colder, usually have lower optical depths, and have smaller particle sizes.

[10] *Hervig et al.* [2001] modeled simulations of the AVHRR response to ice PSCs and cirrus for a range of polar winter conditions (see Figure 12 in the work of *Hervig et al.* [2001] for an example). The modeled PSC and cirrus signals may overlap in some cases, and it was determined that using the cirrus maximum BTD (BTD_{max}) as a threshold to separate ice PSCs from cirrus would yield the most reliable method for identifying PSCs in AVHRR imagery. AVHRR T_5 versus BTD measurements were compared to the modeled ice PSC and cirrus signatures. Ice PSCs are indicated for AVHRR BTD > cirrus BTD_{max}. Using the modeled cirrus BTD_{max} as a threshold to separate cirrus and ice PSCs yields a conservative estimate of ice PSC occurrence.

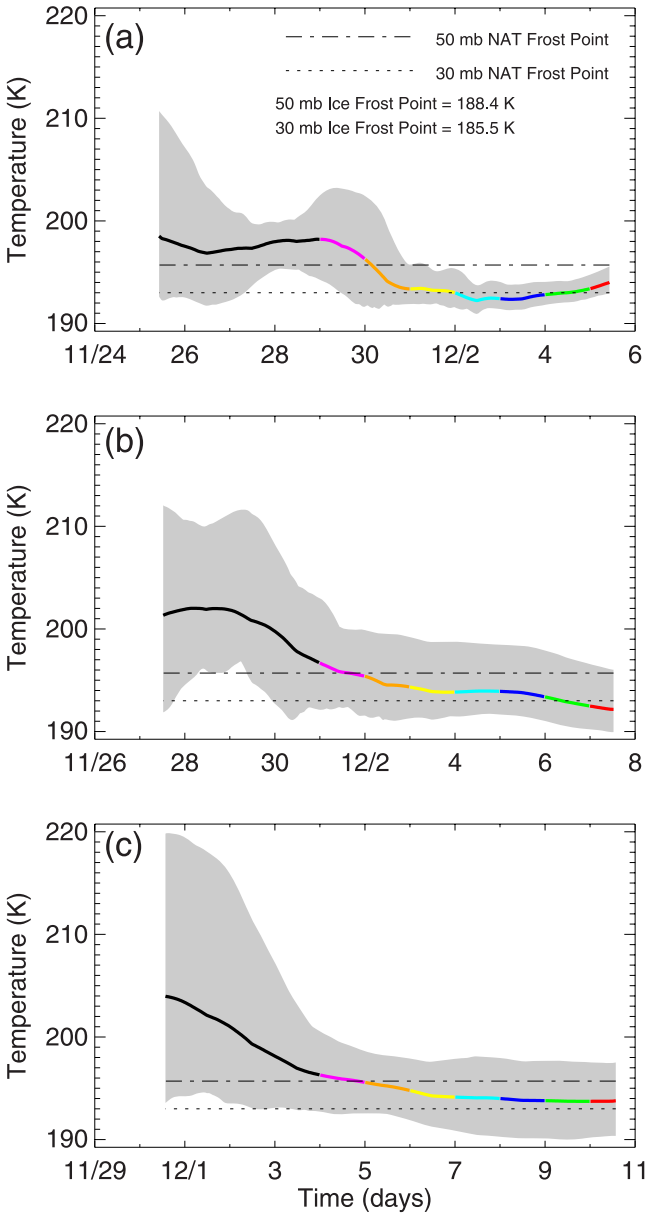

Figure 3. Temperature histories for 10-day back trajectories starting on: (a) 5 December; (b) 7 December; and (c) 10 December 1999. Back trajectories were initialized at the PSC locations shown in Figure 2. The number of trajectories for each PSC is: 15, 50, and 31 for 5, 7, and 10 December, respectively. The gray regions on each plot represent the temperature range for all the trajectories, whereas the thick, colored line represents the mean temperature for all the trajectories. Each color represents one day, as shown on the abscissa. NAT and ice frost points for 30 and 50 hPa were calculated using 5 ppmv H_2O and 10 ppbv HNO_3.

[11] In this study, we used the *Hervig et al.* [2001] AVHRR ice PSC model. Daily T_5 and BTD maps were created from AVHRR 4-km thermal infrared data from the NOAA-14 and NOAA-15 satellites. The T_5 and BTD maps were created by combining all available AVHRR passes for each day. Where pixels overlapped, the minimum T_5 and maximum BTD were chosen as they represent the strongest ice PSC signature. The model also used daily surface temperature (T_{sfc}) and tropopause temperature (T_{trop}) maps. We produced the T_{sfc} maps by interpolating National Center for Environmental Prediction (NCEP) 2.5° × 2.5° daily mean surface temperature reanalysis data to the 4-km AVHRR pixel locations. The T_{trop} maps were produced from 3.75° longitude × 2.5° latitude UKMO 1200 UTC pressure and temperature analysis data. A value of 2.0 potential vorticity units (PVU) was used to identify the tropopause [*Pfister et al.*, 2003]. The T_{trop} data were then interpolated to the 4-km AVHRR pixel locations.

[12] The *Hervig et al.* [2001] AVHRR ice PSC mapping model is a two-step process. First, to identify optically thick ice PSCs, AVHRR T_5 data are compared with UKMO T_{trop} and maximum stratospheric ice frost point temperature (T_{ice}) data on a pixel by pixel basis. In this study, a maximum T_{ice} was calculated assuming a pressure of 150 hPa and 5ppmv H_2O, which yielded a value of ~195 K. AVHRR pixels with $T_5 < T_{trop}$ and BTD > 2.0 or $T_5 < T_{ice}$ and BTD > 2.0 are mapped as ice PSCs. Using the condition BTD > 2.0 eliminates the confusion of cold high clouds with cold earth surfaces, such as ice sheets or sea ice, that have BTDs near zero [*Foschi and Pagan*, 2002]. As the majority of PSCs are optically thin and AVHRR is a nadir-viewing instrument, this step identifies only a small fraction of ice PSCs. For optically thin clouds, AVHRR T_5 is a combination of the cloud and upwelling radiation from below, resulting in a T_5 that is usually warmer than the actual cloud top temperature.

[13] The second step in the model uses BTDs to identify optically thin ice PSCs. In this study, we modeled BTDs for a 2-km thick cirrus layer located at the tropopause, using T_{trop} to estimate the cirrus temperature and T_{sfc} to estimate the underlying surface temperature. We confined T_{trop} to 205 K or the UKMO tropopause temperature, whichever was lower, to assure a realistic but conservative temperature for a tropopause cirrus layer located within the polar vortex. The model yields a series of cirrus BTD curves for each pixel combination of T_{trop} and T_{sfc} that are then compared, pixel by pixel, with AVHRR BTD and T_5 data. AVHRR pixels with BTD > cirrus BTD_{max} are confidently categorized as "ice PSCs." Those pixels with BTD > cirrus BTD_{mean} are labeled as "probable ice PSCs," and pixels with BTD > cirrus BTD_{min} are labeled as "probable tropopause cirrus." Pixels with BTD < cirrus BTD_{min} are labeled as "no PSC." This information is summarized in Table 1, along with the color-coding used for the ice PSC maps described in the next section.

4.2. AVHRR Ice PSC Map and UKMO Back Trajectory Comparisons

[14] Composite AVHRR ice PSC maps for each of the three Type Ia PSC events and associated 10-day back trajectory periods were created. For example, for the 5 December PSC event, we composited the daily ice PSC maps for the period 25 November to 5 December 1999. Where PSC pixels overlapped, we chose the strongest ice PSC signal (i.e., where the criteria in Table 1, from top to bottom, represent the strongest to weakest signature) for that location during the entire 10-day period. These three composite maps showed very little evidence of ice PSCs. Thus we chose to further composite the maps to show ice PSC activity during the period 25 November to 10 December

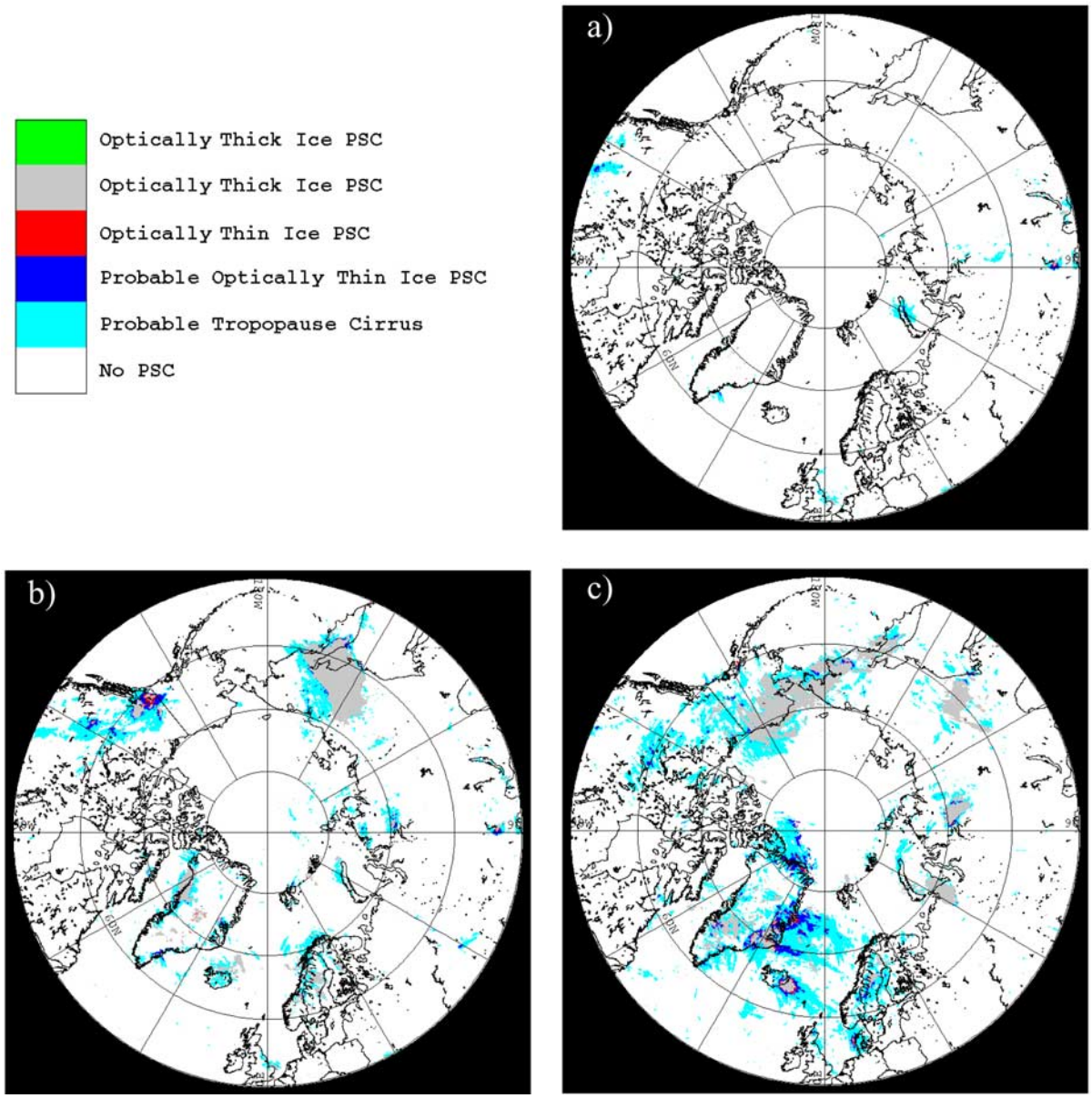

Figure 4. Composite AVHRR ice PSC map for: (a) 25 November to 10 December 1999; (b) 1 December–31 December 1999; and (c) 1 January–31 January 2000. When PSC events overlap during the composite period, the strongest PSC event is mapped. The ice PSC map color-coding is described in Table 1, and the ice PSC statistics are shown in Table 2.

1999 (Figure 4a). This period encompasses all three Type Ia PSC events and associated 10-day back trajectories. Such AVHRR ice PSC maps can represent ice PSCs formed by a variety of means (e.g., synoptic-scale uplift or diabatic cooling, mesoscale mountain-wave activity, nonorographic inertia-gravity waves, etc.). However, AVHRR is particularly suitable for mapping mesoscale mountain-wave cloud events where the rapid cooling produces a large number density of small ice particles that produce large BTDs [*Hervig et al.*, 2001]. Mountain-wave clouds are evidenced

Table 1. Summary of AVHRR Ice PSC Map Categories and Color-Coding

Color	Criteria	PSC Flag
Green	$T_5 < T_{ice}$ and BTD > 2.0	Optically Thick Ice PSC
Gray	$T_5 < T_{trop}$ and BTD > 2.0	Optically Thick Ice PSC
Red	BTD > cirrus BTD_{max}	Optically Thin Ice PSC
Blue	BTD > cirrus BTD_{mean}	Probable Optically Thin Ice PSC
Cyan	BTD > cirrus BTD_{min}	Probable Tropopause Cirrus
White	BTD < cirrus BTD_{min} and $T_5 > T_{trop}$	No PSC
Black	No AVHRR Data	No PSC

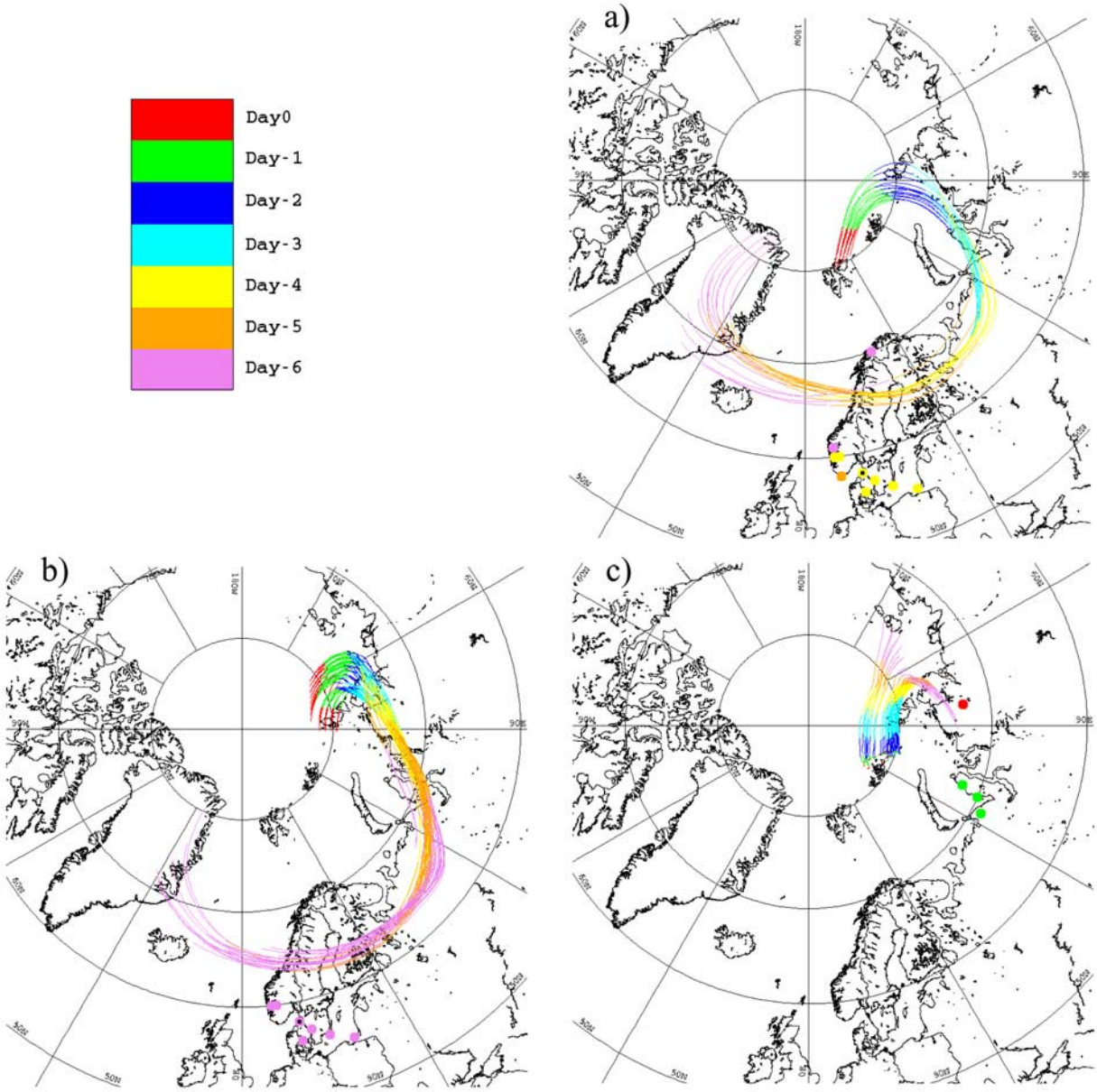

Figure 5. UKMO back trajectory paths and 0000 UTC grid box averaged MWFM-2 wave temperature amplitude hindcast data for locations with cooling below the ice frost point for: (a) 29 November to 5 December 1999; (b) 1 December to 7 December 1999; and (c) 4 December to 10 December 1999. Six-day back trajectories and MWFM-2 $T_{DAO} - T_{RMS} - T_{\sigma}$ data are overlaid in color: red, green, blue, cyan, yellow, orange, and pink indicate Day0 through Day-6, respectively. Note that the MWFM-2 points and back trajectory paths are color-coordinated. Thus for a MWFM-2 point to overlap temporally and spatially with a back trajectory path, they must have the same color. The only MWFM-2 $T_{DAO} - T_{RMS} - T_{\sigma} - 3$ K point (associated with cooling sufficient to lower the air temperature at least 3 K below the ice frost point) is indicated with a small black dot. All the MWFM-2 data points are located at 30 hPa.

in AVHRR as high cirrus or ice PSCs over and downwind of mountainous terrain.

[15] The ice PSC map shown in Figure 4a indicates that very little ice PSC activity occurred during 25 November to 10 December 1999. Some small regions of localized mountain-wave cloud activity were noted, for example, off the southeast coast of Greenland and over Novaya Zemlya. Our analysis shows that these mountain-wave clouds were most likely tropospheric (i.e., colored cyan, probable tropopause cirrus) with only a minimal number of pixels representing ice PSCs or probable ice PSCs (red and dark blue on the map). We compared the path of the back trajectories for each Type Ia PSC event (Figure 5) with the ice PSC locations in Figure 4a. In none of the three cases did the

Table 2. Statistics for Ice PSC Maps in Figure 4 for 25 November to 10 December 1999 (Figure 4a); 1 December to 31 December 1999 (Figure 4b); and 1 January to 31 January 2000 (Figure 4c)[a]

Color	PSC Flag	Figure 4a Coverage, %	Figure 4b Coverage, %	Figure 4c Coverage, %
Green	Optically Thick Ice PSC	<0.001	<0.001	<0.001
Gray	Optically Thick Ice PSC	0.004	2.542	4.304
Red	Optically Thin Ice PSC	0.002	0.076	0.148
Blue	Probable Optically Thin Ice PSC	0.038	0.314	0.923
Cyan	Probable Tropopause Cirrus	0.550	4.016	8.467
White	No PSC	99.407	93.051	86.158

[a]Coverage (%) is defined as the percentage of pixels that fall into each class within the region from 50° to 90°N.

air parcels travel through any category of ice PSCs prior to the lidar detection of the NAT clouds.

4.3. AVHRR and Mountain-Wave Cloud PSC Climatology Comparison

[16] *Dörnbrack et al.* [2001] compared Penn State/National Center for Atmospheric Research Mesoscale Model (MM5) mesoscale fields with European Center for Medium-Range Weather Forecasts (ECMWF) synoptic-scale analyses and remote sensing and in situ observations over northern Scandinavia for one month, January 1997. From this study, they developed a set of dynamic criteria for stratospheric mountain-wave cloud activity over Scandinavia based on low-level (900 hPa) wind speed and direction and the directional shear between low-level (900 hPa) and high-level (500 to 50 hPa) winds.

[17] *Dörnbrack and Leutbecher* [2001] used the dynamic criteria described above to develop a 20-year seasonal (1979–1980 to 1998–1999) climatology of potential PSC formation at 30, 50, and 70 hPa over Scandinavia. Based on an analysis of this 20-year climatology, they concluded that: (1) Type II PSCs are less likely to form than Type I PSCs; (2) Type II PSC formation was dominated by mesoscale cooling events on the order of 2–8 K; and (3) Type II PSCs have the highest potential to form in January and February and have the lowest potential for formation in December and March.

[18] Composite AVHRR ice PSC maps for 25 November to 10 December 1999, 1 December to 31 December 1999, and 1 January to 31 January 2000 are shown in Figure 4. PSC statistics for each of these maps are shown in Table 2. The AVHRR ice PSC statistics reveal that within the area from 50° to 90° N, ice PSCs (all categories on the map except for "Probable Tropopause Cirrus," colored cyan) covered ~0.05% of the region from 25 November to 10 December 1999, ~2.9% of the region in December 1999, and ~5.4% of the region in January 2000. These statistics represent areal coverage and not frequency, and they represent ice clouds for all levels in the stratosphere. PSC frequency for a given location can be determined by computing the number of times each pixel fell into an ice PSC category on each day during the period of interest. We did not attempt to do this analysis for this study. However, a visual inspection of the daily AVHRR ice PSC maps revealed that ice PSCs formed more often over Greenland and Scandinavia (regions associated with high-amplitude mountain-wave activity) during January 2000 than in December 1999.

[19] Although AVHRR has excellent temporal and horizontal resolution, it is difficult to determine the exact altitude of the ice PSCs. For optically thick PSCs, T_5 can be used as a conservative estimate of cloud top temperature and can therefore be compared to temperature analyses or radiosonde data to estimate the vertical position of the cloud. Determining the vertical placement of optically thin PSCs is more difficult. For these clouds, the *Hervig et al.* [2001] model uses the BTD criteria. We use a conservative value of T_{trop} (205 K or UKMO, whichever is less), and this ensures that the clouds mapped as ice PSCs are in the stratosphere. Future work on the AVHRR ice PSC model will include methods to estimate the temperature of optically thin ice PSCs, which will help to determine their altitude within the stratosphere.

[20] A direct comparison of the AVHRR ice PSC data with the ice PSC climatology data derived by *Dörnbrack and Leutbecher* [2001] is not possible. The AVHRR PSCs extend over a wider altitude range and a larger areal extent. The PSC mountain-wave climatology statistics are limited to northern Scandinavia and cover only 30–70 hPa. Furthermore, the AVHRR ice PSC statistics represent PSC areal coverage, whereas the PSC mountain-wave climatology statistics represent frequency of PSC formation potential. Nevertheless, the AVHRR ice PSC statistics show that a larger region of ice PSCs formed in January than in December (with a visual inspection of daily ice PSC maps indicating they also formed more often in January), which is in agreement with the trend in the ice PSC climatology statistics derived by *Dörnbrack and Leutbecher* [2001]. While the AVHRR ice PSC maps in Figure 4 represent a combination of PSC formation dynamics, there are regions of obvious mountain-wave cloud activity. These regions are in alignment with preferred regions of mountain-wave cloud activity for other PSC seasons, such as those shown by *Carslaw et al.* [1998], and show a marked increase from December to January.

5. AVHRR and MWFM-2 Type II PSC Comparisons

[21] To provide further evidence that the three Type Ia PSCs observed in early December 1999 did not form by heterogeneous nucleation of NAT on ice particles generated in mountain waves, we performed MWFM-2 hindcasts [*Eckermann and Preusse*, 1999; *Bacmeister et al.*, 1994; *Jiang et al.*, 2004] to identify locations where stratospheric mountain-wave activity was predicted to cool synoptic-scale temperatures below the ice frost point. We then overlaid the back trajectory paths on the MWFM-2 hindcast maps to determine whether the air parcels traveled through regions

of high-amplitude mountain-wave activity prior to the time the DC-8 lidar observed the NAT clouds.

[22] The MWFM uses a detailed parameterization approach to forecast/hindcast the geographical locations and amplitudes of mountain waves in the troposphere and stratosphere, as well as wave-induced effects such as turbulence or wave-cloud formation. Briefly, the MWFM "postprocesses" large-scale atmospheric winds and temperatures generated either by numerical weather prediction models (MWFM forecast mode) or data assimilation systems (MWFM hindcast mode) to estimate the subgrid-scale mountain wave content for a particular atmospheric environment. Surface winds are "blown" over a collection of diagnosed ridges which define major topographic structures over the globe relevant to mountain-wave forcing, and a set of forced mountain waves is generated. Wind and temperature profiles above the parent ridge are then used to model the radiation of these mountain waves away from the ridge feature, including tracking of wave amplitudes along the wave's group propagation path.

[23] *Bacmeister et al.* [1994] describe the formulation and first results of Version 1 of the model (MWFM-1), which used a two-dimensional hydrostatic irrotational gravity wave formation. In this study, we use Version 2 of the MWFM (MWFM-2), which employs a three-dimensional nonhydrostatic rotational ray-tracing formulation to more accurately specify both horizontal and vertical group propagation of wave energy away from parent ridges. The MWFM-2 was used to forecast mountain waves during SOLVE-THESEO 2000 and was used by *Hertzog et al.* [2002] to hindcast and study a stratospheric mountain wave measured by balloon over southern Scandinavia on 2 March 2000.

[24] Whereas MWFM-1 generates a single plane hydrostatic wave over any given ridge feature, MWFM-2 launches a collection of rays of different horizontal wavenumbers and wave azimuths from each parent ridge. The raw hemispheric ray data generated by MWFM-2 are voluminous and, as such, can be impractical for certain applications. For example, *Pierce et al.* [2003] chose to average the raw ray data from MWFM-2 hindcasts of wave temperature amplitudes in their chemical transport model (CTM) study in order to yield a more tractable mean mountain wave contribution within a grid box that could be easily ingested into their CTM calculations. Their approach was to compute root mean square (r.m.s.) peak mountain-wave temperature amplitudes, T_{RMS}, as well as standard deviations based on all the MWFM-2 ray data at a given altitude within a given $1^\circ \times 1^\circ$ grid box, T_σ, as hindcast by MWFM-2 using the NASA Data Assimilation Office (DAO) 0000 UTC analyses. We used the same grid box averaged MWFM-2 data as described above (also see section 6 of *Pierce et al.* [2003]) to characterize a mean mountain-wave temperature perturbation within each $1^\circ \times 1^\circ$ grid box for pressure levels ranging from 100 to 10 hPa. The ray launch parameters we used follow those described in section 3.2.3 of *Hertzog et al.* [2002], except we used two instead of three different horizontal wavenumbers, launched at 18 azimuths successively rotated by 10° to span a full 180° downwind of the ridge axis (see also *Jiang et al.* [2004]).

[25] We calculated ice frost point temperatures for 30, 40, and 50 hPa (assuming 5 ppmv H_2O), corresponding to the range of pressure levels for the three NAT clouds and associated back trajectories. We used the grid box averaged MWFM-2 0000 UTC hindcast wave temperature amplitude data along with DAO 0000 UTC mean temperature analysis data (T_{DAO}) to locate regions of predicted ice PSC formation from 50° to 90°N. First, we computed $T_{DAO} - T_{RMS}$ values for the period 25 November to 10 December 1999. No day during that time period experienced sufficient mountain-wave activity to cool the air below the ice frost point. This result is in agreement with the AVHRR results discussed previously, which showed no evidence of ice PSCs at or downwind of mountainous terrain.

[26] Next, to investigate a broader set of possible mountain-wave cooling events, we computed $T_{DAO} - T_{RMS} - T_\sigma$ for the same time period. This yielded only 16 data points (all at 30 hPa), with almost half (seven) occurring on 1 December 1999. These data points were plotted along with the 6-day back trajectory paths for each of the three PSC events in early December 1999 (Figure 5). We used 6-day back trajectories because, in these three cases, the synoptic-scale temperatures were too warm to sustain a Type Ia PSC formed more than 6 days earlier. Note that the circles in Figure 5 which represent locations where grid box averaged MWFM-2 data predict mountain-wave cooling below the ice frost point are color-coordinated with the back trajectory paths. Thus for a trajectory path to overlap a MWFM-2 point in time and space, they must have the same color. A visual inspection of the back trajectory and grid box averaged MWFM-2 wave temperature amplitude data in Figure 5 shows virtually no spatial or temporal correlation between the two data sets. None of the back trajectory data overlaps a MWFM-2 point, and the nearest coincidence is at least 500 km away and occurs on only 2 days.

[27] *Carslaw et al.* [1998] and *Chang et al.* [1999] have suggested that air temperatures need to drop 3 to 4 K below the ice frost point for ice nucleation to occur. Thus we subtracted 3 K from the grid box averaged MWFM-2 $T_{DAO} - T_{RMS} - T_\sigma$ data to determine if any of the mountain-wave cooling events described above were sufficient to initiate ice nucleation. Only one data point, on 1 December 1999, met this criterion and is noted in Figure 5 as a yellow or pink circle with a black dot.

[28] The results of the comparisons between the synoptic-scale back trajectory data and the grid box averaged MWFM-2 wave temperature amplitude hindcast data (for all three scenarios: $T_{DAO} - T_{RMS}$, $T_{DAO} - T_{RMS} - T_{\sigma,}$ and $T_{DAO} - T_{RMS} - T_\sigma - 3$ K) show that mountain-wave activity was not sufficient to produce cooling to or below the ice frost point needed to initiate Type II PSC formation. These results are in agreement with our AVHRR ice PSC analysis.

[29] We explored the possibility that the grid box averaged MWFM-2 wave temperature amplitude data used above may not be the most appropriate metric to predict ice formation. The grid box averaging procedure can eliminate much of the structure and variability contained within the original hindcast, particularly when there are a large number of rays in a given grid box that have tiny amplitudes. Thus depending upon the spectrum of waves present at a location, the coldest local temperatures, which

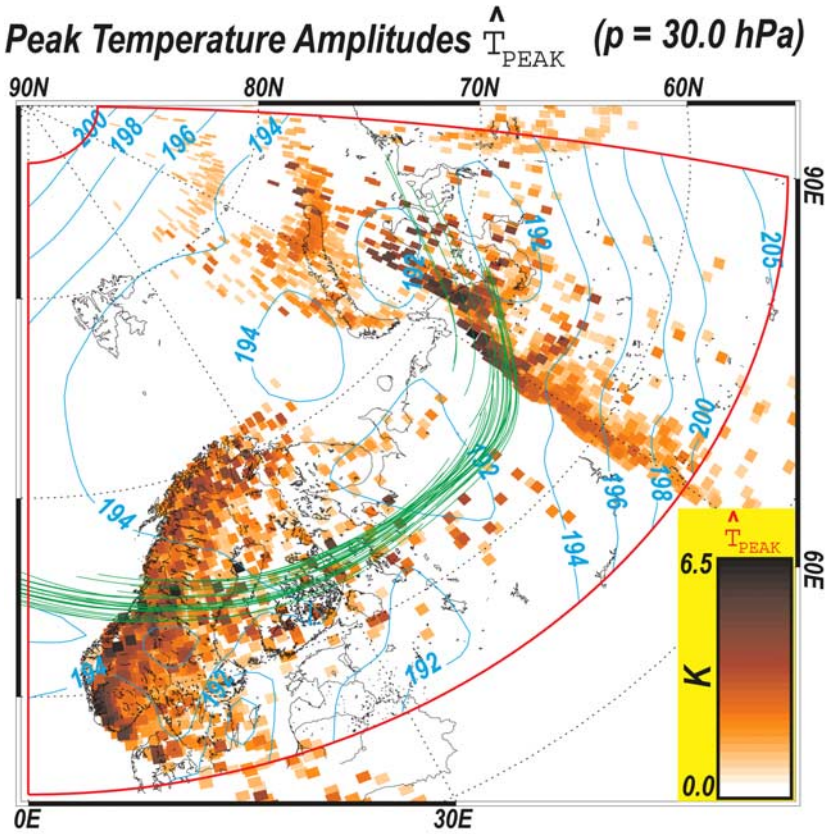

Figure 6. MWFM-2 hindcast of peak mountain wave temperature amplitudes at 30 hPa on 1 December 1999 at 1200 UTC, derived from the DAO "first-look" analysis. Each square pixel (width 0.5° × 1°) represents the group location and amplitude of a mountain wave ray (see attached color bar; scale is linear). Pixels are plotted in order of ascending amplitude; thus in regions with many colocated rays, the largest amplitude rays are plotted on top of the smaller amplitude ones, since only the largest amplitude rays are significant microphysically. Synoptic-scale DAO analysis temperatures (K) are contoured in cyan, while trajectories for this date from Figure 5b are overplotted in green. Red border shows the region within which MWFM-2 performed a forecast.

are most relevant to the ice formation potential, could potentially be more extreme than $T_{DAO} - T_{RMS} - T_{\sigma}$.

[30] For the period 25 November to 10 December, the grid box averaged data had the strongest signature for mountain-wave cooling sufficient to lower the synoptic-scale temperatures to or below the ice frost point on 1 December 1999. We analyzed 0000 and 1200 UTC MWFM-2 raw (unaveraged) hemispheric ray hindcast data for 1 December 1999 and then compared the raw data with the grid box averaged data for that day. MWFM-2 produces a voluminous output of raw hemispheric ray data, which makes a point-by-point comparison of these data with AVHRR and back trajectory data impractical. Rather, we generated hindcast maps of peak temperature amplitudes (similar to those shown in Figure 8 of *Hertzog et al.* [2002]) at 30, 40, and 50 hPa and compared them with our earlier trajectory analyses. The 30 hPa hindcast of peak temperature amplitudes for 1 December 1999 at 1200 UTC is shown in Figure 6, for a geographical subregion corresponding to the location of the back trajectory data for this date. The 1 December locations of the back trajectories corresponding to the 7 December 1999 Type Ia PSC are shown in green in Figure 6. The largest peak amplitude temperature cooling at 1200 UTC for 1 December at 30 hPa was ~6.5 K (dark red and black on the temperature color scale in Figure 6). The majority of the pixels (rays) show cooling less than 6.0 K. We then compared the ice frost point temperature for 30 hPa (185.5 K, using 5ppmv H_2O) with the 1200 UTC DAO temperature field (cyan contours on Figure 6). We determined that there was not sufficient mountain-wave cooling to lower the synoptic-scale temperatures below the ice frost point. Furthermore, an additional 3–4 K cooling would be needed to initiate ice nucleation. Similar comparisons of 1200 UTC MWFM-2 peak temperature amplitude data with 1200 UTC DAO synoptic scale temperatures for 40 and 50 hPa yielded the same conclusion. We also note that the 1 December locations of the back trajectories corresponding to the 5 December 1999 Type Ia PSC (Figure 5a) are located slightly north of the trajectories shown in Figure 6. Thus our discussion above also holds true for the 5 December 1999 PSC event.

[31] The grid box averaged MWFM-2 wave temperature amplitude hindcast data for 0000 UTC on 1 December 1999 (Figures 5a and 5b) did show seven locations where mountain-wave activity cooled the air temperature below the ice frost point, of which one location was at least 3 K

below the ice frost point. We compared the back trajectory locations for 1 December with the 0000 UTC MWFM-2 raw (unaveraged) hemispheric ray hindcast data for 30, 40, and 50 hPa and determined that the 0000 UTC MWFM-2 raw data also showed cooling below the ice frost point in roughly the same region as shown in Figures 5a and 5b, with only a few locations at 30 hPa with cooling at least 3 K below the ice frost point. As was the case with the grid box averaged MWFM-2 wave temperature amplitude data shown in Figures 5a and 5b, the small regions of localized cooling in the raw data were ~500 km south of the back trajectories.

[32] The results of the analysis of MWFM-2 hindcast data, using both the raw hemispheric ray data and the grid box averaged data, show strong evidence that ice particles formed in regions of mountain-wave activity in the stratosphere were not a factor in the formation of the three NAT clouds measured by the DC-8 lidar in early December 1999. When compared with back trajectory locations, the cooling associated with mountain-wave activity in early December was not sufficient to lower synoptic-scale temperatures to or below the ice frost point and initiate ice nucleation. It is likely that the grid box averaged MWFM-2 hindcast data underestimates the mountain-wave cooling, whereas the raw hemispheric ray data better match or slightly overestimate the wave cooling [e.g., *Eckermann and Preusse*, 1999; *Hertzog et al.*, 2002]. Thus it is likely that the actual cooling associated with mountain-wave activity is somewhere between these two limits. In our case, both MWFM hindcast data sets show insufficient cooling to initiate ice clouds and are therefore in agreement with the AVHRR data which show no evidence of ice PSCs at or close to the three NAT cloud back trajectory locations.

6. Discussion and Conclusions

[33] The analysis presented in this paper shows strong evidence that the three Type Ia PSCs measured by the DC-8 lidar in the Arctic vortex during early December 1999 were not formed as a result of heterogeneous nucleation of NAT on ice particle surfaces in regions of stratospheric mountain-wave activity. The analysis of AVHRR data showed scant evidence of ice PSC formation during 25 November to 10 December 1999. The AVHRR ice PSCs statistics for this period are in agreement with ice PSC climatology statistics derived by *Dörnbrack and Leutbecher* [2001]. Comparisons of AVHRR ice PSC locations with UKMO back trajectories initialized at locations where the DC-8 lidar observed the NAT clouds show no evidence that the air passed through regions of Type II PSCs formed by stratospheric mountain-wave activity prior to the NAT cloud observations. Furthermore, an analysis of MWFM-2 hindcast wave temperature amplitude data did not show evidence of sufficient cooling to lower synoptic-scale temperatures to or below the ice frost point to initiate ice nucleation.

[34] Based on our analysis, we conclude that Type Ia PSCs can nucleate in relatively warm synoptic-scale temperature fields and are not limited to forming at or downwind of regions of strong mountain-wave activity with sufficient cooling to produce ice nuclei. Our conclusion does not concur with a prevailing theory that Type Ia PSCs only form, or most likely form, by heterogeneous nucleation of NAT on ice particles in regions of stratospheric mountain-wave activity [*Carslaw et al.*, 1998, 1999; *Zondlo et al.*, 2000; *Füglistaler et al.*, 2002a, 2002b; *Dhaniyala et al.*, 2002; *Luo et al.*, 2003; *Voight et al.*, 2003.]

[35] *Hitchman et al.* [2003] suggest that the Type Ia PSC detected on 7 December 1999 was formed due to cooling associated with nonorographic inertia-gravity waves generated by breaking synoptic-scale tropospheric Rossby waves along the polar front jet, which propagate into the stratosphere. We generated MWFM-2 raw hemispheric ray hindcast data for 7 December 1999 and overlaid DAO synoptic-scale temperatures on the MWFM-2 maps. The MWFM-2 raw data showed no evidence of mountain-wave activity in the region of the observed Type Ia PSC. The cooling associated with the inertia-gravity wave described by *Hitchman et al.* [2003] was at most ~3 K. The 7 December DAO synoptic-scale temperature fields for 30, 40, and 50 hPa at the location of the observed Type Ia PSC were ~4–7 K above the ice frost point temperature. Thus cooling on the order of ~3 K would not be sufficient to lower the synoptic-scale temperatures to, or 3 K below, the ice frost point. While nonorographic inertia-gravity waves may play a role in the generation of Type Ia PSCs, in this case, the Type Ia PSC observed on 7 December 1999 did not form by heterogeneous nucleation of NAT on ice particles, but rather by some other nucleation mechanism.

[36] It is beyond the scope of this paper to provide a detailed analysis of other nucleation mechanisms that might be responsible for the formation of the three NAT clouds observed in the Arctic vortex in early December 1999. However, we provide a brief summary of possible nucleation mechanisms as follows.

[37] We explored the possibility of homogeneous freezing as a mechanism for the formation of the three NAT clouds. We calculated hourly solid particle production rates for volume-based nucleation modes [*Salcedo et al.*, 2001] and surface-based nucleation modes [*Tabazadeh et al.*, 2002]. The synoptic-scale trajectories shown in Figure 3 indicate that the air parcels spent roughly five days in the mean temperature range of 192–195 K for all three PSCs. In this temperature range, and at pressures ranging from 30–50 hPa, neither the *Salcedo et al.* [2001] homogeneous volume nucleation rates nor the *Tabazadeh et al.* [2002] surface nucleation rates can produce solid NAD particles. Further calculations showed that temperatures would need to lower to 189 K (at 30 hPa) and 191 K (at 50 hPa) for homogeneous nucleation to begin. The surface-based nucleation mode would require a few hours of air mass exposure at these lower temperatures to yield a sufficient number of NAD nuclei in the air for the lidar to observe the particles; the volume-based nucleation mode would require several days' exposure at these lower temperatures to yield a cloud. The lower temperatures needed for NAD particle production may be explained by temperature uncertainties in the synoptic-scale temperature analyses and back trajectory calculations or by small-amplitude mesoscale fluctuations. We note that direct homogeneous nucleation of NAT based on current nucleation rates [*Salcedo et al.*, 2001; *Tabazadeh et al.*, 2002] is insufficient by itself to produce enough solid particles in the air for lidar to detect these Type Ia PSCs. Thus based on the discussion above, taking temperature uncertainties and

small-amplitude mesoscale fluctuations into account, surface-based homogeneous nucleation of NAD particles that later on convert to NAT cannot be excluded as a possible mechanism for the formation of the three Type Ia PSCs observed in early December 1999.

[38] Other possibilities for NAT cloud formation may include heterogeneous nucleation on exotic solid nuclei [*Drdla et al.*, 2003; *Tolbert and Toon*, 2001]. However, no published rates are currently available to quantitatively determine if heterogeneous nucleation on exotic nuclei can explain the occurrence of these clouds in early winter.

[39] Whatever nucleation process was responsible for the formation of the three NAT clouds in the relatively warm synoptic-scale environment in early December 1999 should also operate efficiently when synoptic-scale temperature fields are significantly colder, such as in January 2000. We have provided strong evidence that heterogeneous nucleation of NAT on ice particles generated in regions of mountain-wave activity cannot be the sole mechanism for Type Ia PSC formation in the Arctic vortex. We plan to repeat our analysis technique for January 2000 to determine what percentage of Type Ia PSCs observed during the SOLVE campaign can be linked to mountain-wave activity upstream. Furthermore, *Strawa et al.* [2002] have developed a method to discriminate Type Ia from Type Ib PSCs in Polar Ozone and Aerosol Measurement (POAM) data. This method is also applicable to Stratospheric Aerosol and Gas Experiment (SAGE) data as well. These data sets can provide a long-term record of Type Ia PSCs that can be analyzed using AVHRR ice PSC data and back trajectory data to help determine whether ice particles generated in regions of mountain-wave activity play a dominant role in the formation of NAT clouds in the Arctic vortex.

[40] **Acknowledgments.** This work was supported by the NASA ACMAP and the NASA UARS projects. The AVHRR data were acquired through the NOAA Satellite Active Archive. We thank Leonhard Pfister for the many helpful conversations regarding various aspects of this paper.

References

Bacmeister, J. T., P. A. Newman, B. L. Gary, and K. R. Chan (1994), An algorithm for forecasting mountain wave-related turbulence in the stratosphere, *Weather Forecasting*, *9*, 241–253.

Browell, E. V., et al. (1990), Airborne lidar observations in the wintertime Arctic stratosphere: Polar stratospheric clouds, *Geophys. Res. Lett.*, *17*(4), 385–388.

Carslaw, K. S., M. Wirth, A. Tsias, B. P. Luo, A. Dörnbrack, M. Leutbecher, H. Volkert, W. Renger, J. T. Bacmeister, and T. Peter (1998), Particle microphysics and chemistry in remotely observed mountain polar stratospheric clouds, *J. Geophys. Res.*, *103*(D5), 5785–5796.

Carslaw, K. S., T. Peter, J. T. Bacmeister, and S. D. Eckermann (1999), Widespread solid particle formation by mountain waves in the Arctic stratosphere, *J. Geophys. Res.*, *104*(D1), 1827–1836.

Chang, H. A., T. Koop, L. T. Molina, and M. J. Molina (1999), Phase transition in emulsified HNO_3/H_2O and $HNO_3/H_2SO_4/H_2O$ solutions, *J. Phys. Chem.*, *103*, 2673–2679.

Dhaniyala, S., K. A. McKinney, and P. O. Wennberg (2002), Lee-wave clouds and denitrification of the polar stratosphere, *Geophys. Res. Lett.*, *29*(9), 1322, doi:10.1029/2001GL013900.

Dörnbrack, A., and M. Leutbecher (2001), Relevance of mountain wave cooling for the formation of polar stratospheric clouds over Scandinavia: A 20 year climatology, *J. Geophys. Res.*, *106*(D2), 1583–1593.

Dörnbrack, A., M. Leutbecher, J. Reichardt, A. Behrendt, K. Müller, and G. Baumgarten (2001), Relevance of mountain wave cooling for the formation of polar stratospheric clouds over Scandinavia: Mesoscale dynamics and observations for January 1997, *J. Geophys. Res.*, *106*(D2), 1569–1581.

Drdla, K., M. R. Schoeberl, and E. V. Browell (2003), Microphysical modeling of the 1999–2000 Arctic winter: 1. Polar stratospheric clouds, denitrification, and dehydration, *J. Geophys. Res.*, *108*(D5), 8312, doi:10.1029/2001JD000782.

Eckermann, S. D., and P. Preusse (1999), Global measurements of stratospheric mountain waves from space, *Science*, *286*, 1534–1537.

Foschi, P. G., and K. L. Pagan (2002), Toward a polar stratospheric cloud climatology using advanced very high resolution radiometer thermal infrared data, *Can. J. Remote Sens.*, *28*(2), 187–195.

Füglistaler, S., B. P. Luo, C. Voight, K. S. Carslaw, and T. Peter (2002a), NAT-rock formation by mother clouds: A microphysical model study, *Atmos. Chem. Phys.*, *2*, 93–98.

Füglistaler, S., et al. (2002b), Large NAT particle formation by mother clouds: Analysis of SOLVE/THESEO-2000 observations, *Geophys. Res. Lett.*, *29*(12), 1610, doi:10.1029/2001GL014548.

Garcia, O., K. L. Pagan, P. G. Foschi, S. Gaines, and R. S. Hipskind (1995), Detection of polar stratospheric clouds over Antarctica using AVHRR images obtained at Palmer Station during August 1992, *Polar Rec.*, *31*, 211–226.

Hertzog, A., F. Vial, A. Dörnbrack, S. D. Eckermann, B. M. Knudsen, and J. P. Pommereau (2002), In situ observations of gravity waves and comparisons with numerical simulations during the SOLVE/THESEO 2000 campaign, *J. Geophys. Res.*, *107*(D20), 8292, doi:10.1029/2001JD001025.

Hervig, M. E., K. L. Pagan, and P. G. Foschi (2001), Analysis of PSC measurements from AVHRR, *J. Geophys. Res.*, *106*(D10), 10,363–10,374.

Hitchman, M. H., M. L. Bucker, G. J. Tripoli, E. V. Browell, W. B. Grant, T. J. McGee, and J. F. Burris (2003), Nonorographic generation of Arctic polar stratospheric clouds during December 1999, *J. Geophys. Res.*, *108*(D5), 8325, doi:10.1029/2001JD001034.

Jiang, J. H., S. D. Eckermann, D. L. Wu, and J. Ma (2004), A search for mountain waves in MLS stratospheric limb radiance from the Northern Hemisphere: Data analysis and global mountain wave modeling, *J. Geophys. Res.*, *109*, doi:10.1029/2003JD003974, in press.

Kidder, S. Q., and T. H. Vonder Haar (1995), Meteorological satellite instrumentation, in *Satellite Meteorology: An Introduction*, pp. 87–97, Academic, San Diego, Calif.

Luo, B. P., C. Voight, S. Füglistaler, and T. Peter (2003), Extreme NAT supersaturation in mountain wave ice PSCs: A clue to NAT formation, *J. Geophys. Res.*, *108*(D15), 4441, doi:10.1029/2002JD003104.

Manney, G. L., et al. (2003), Lower stratospheric temperature differences between meteorological analyses in two cold Arctic winters and their impact on polar processing studies, *J. Geophys. Res.*, *108*(D5), 8328, doi:10.1029/2001JD001149.

Pagan, K. L. (1996), Detection of polar stratospheric clouds over Antarctica using AVHRR satellite imagery, M.S. thesis, San Francisco State Univ., San Francisco, Calif.

Pfister, L. H., et al. (2003), Processes controlling water vapor in the winter Arctic tropopause region, *J. Geophys. Res.*, *108*(D5), 8314, doi:10.1029/2001JD001067.

Pierce, R. B., et al. (2003), Large-scale chemical evolution of the Arctic vortex during the 1999/2000 winter: HALOE/POAM III Lagrangian photochemical modeling for the SAGE III Ozone Loss and Validation Experiment (SOLVE) campaign, *J. Geophys. Res.*, *108*(D5), 8317, doi:10.1029/2001JD001063.

Salcedo, D., L. T. Molina, and M. J. Molina (2001), Homogeneous freezing of concentrated aqueous nitric acid solutions at polar stratospheric temperatures, *J. Phys. Chem.*, *105*(9), 1433–1439.

Strawa, A. W., et al. (2002), Discriminating Types Ia and Ib polar stratospheric clouds in POAM satellite data, *J. Geophys. Res.*, *107*(D20), doi:10.1029/2001JD000458.

Tabazadeh, A., O. B. Toon, B. L. Gary, J. T. Bacmeister, and M. R. Schoeberl (1996), Observational constraints on the formation of Type Ia polar stratospheric clouds, *Geophys. Res. Lett.*, *23*(16), 2109–2112.

Tabazadeh, A., E. J. Jensen, O. B. Toon, K. Drdla, and M. R. Schoeberl (2001), Role of the stratospheric polar freezing belt in denitrification, *Science*, *291*, 2591–2594.

Tabazadeh, A., Y. S. Djikaev, P. Hamill, and H. Reiss (2002), Laboratory evidence for surface nucleation of solid polar stratospheric cloud particles, *J. Phys. Chem.*, *106*, 10,238–10,246.

Teitelbaum, H., M. Moustaoui, and M. Fromm (2001), Exploring polar stratospheric cloud and ozone minihole formation: The primary importance of synoptic-scale flow perturbations, *J. Geophys. Res.*, *106*(D22), 28,173–28,188.

Tolbert, M. A., and O. B. Toon (2001), Atmospheric science: Enhanced: Solving the PSC mystery, *Science*, *292*, 61–63.

Toon, O. B., A. Tabazadeh, E. V. Browell, and J. Jordan (2000), Analysis of lidar observations of Arctic polar stratospheric clouds during January 1989, *J. Geophys. Res.*, *105*(D16), 20,589–20,615.

Voight, C., et al. (2003), In situ mountain-wave polar stratospheric cloud measurements: Implications for nitric acid trihydrate formation, *J. Geophys. Res.*, *108*(D5), 8331, doi:10.1029/2001JD001185.

World Meteorological Organization (2003), Scientific assessment of ozone depletion: 2002, *Rep. 47*, 498 pp., Global Ozone Res. and Monit. Proj., Geneva.

Zondlo, M. A., P. K. Hudson, A. J. Prenni, and M. A. Tolbert (2000), Chemistry and microphysics of polar stratospheric clouds and cirrus clouds, *Annu. Rev. Phys. Chem.*, *51*, 473–499.

E. V. Browell, NASA Langley Research Center, Mail Stop 401A, Hampton, VA 23681-2199, USA. (edward.v.browell@nasa.gov)

K. Drdla and A. Tabazadeh, NASA Ames Research Center, MS 245-4, Moffett Field, CA 94035-1000, USA. (katja.drdla-1@nasa.gov; azadeh.tabazadeh-1@nasa.gov)

S. D. Eckermann, Middle Atmospheric Dynamic Section, E. O. Hulbert Center for Space Research, Naval Research Laboratory, Code 7646, Washington, DC 20375-5352, USA. (stephen.eckermann@nrl.navy.mil)

P. G. Foschi, Romberg Tiburon Center for Environmental Studies, San Francisco State University, 3152 Paradise Drive, Tiburon, CA 94920-1205, USA. (tfoschi@sfsu.edu)

M. E. Hervig, G & A Technical Software, Inc., P. O. Box 449, Driggs, ID 83422, USA. (m.e.hervig@gats-inc.com)

M. J. Legg and K. L. Pagan, NASA Ames Research Center, MS 245-5, Moffett Field, CA 94035-1000, USA. (legg@pixels.arc.nasa.gov; pagan@cloud1.arc.nasa.gov)